Final Draft
of the original manuscript:

Stanev, E.V.; Grayek, S.; Claustre, H.; Schmechtig, C.; Poteau, A.:
Water intrusions and particle signatures in the Black Sea: A Biogeochemical-Argo float investigation
In: Ocean Dynamics (2017) Springer

DOI: 10.1007/s10236-017-1077-9

Water intrusions and particle signatures in the Black Sea: a Biogeochemical-Argo float investigation

E.V. Stanev[1, 2], S. Grayek[1], H. Claustre[3], C. Schmechtig[3], and A. Poteau[3]

[1]Institute of Coastal Research, Helmholtz-Zentrum Geesthacht, Max-Planck-Strasse 1, 21502 Geesthacht, Germany.

[2]Department of Meteorology and Geophysics, University of Sofia, 5 James Bourchier Street, 1126 Sofia, Bulgaria.

[3]Sorbonne Universités, UPMC Univ Paris 06, CNRS-INSU, UMR 7093, Laboratoire d'Océanographie de Villefranche-sur-mer (LOV), 06230 Villefranche-sur-mer,France.

Corresponding author: Emil Stanev (emil.stanev@hzg.de)

Abstract

Continuous observations during three years with a vertical resolution of 1 dbar from two Bio-Argo floats in the Black Sea that were equipped with oxygen optodes, chlorophyll fluorometers, and backscattering sensors are analyzed. The particle backscattering coefficient, b_{bp} provides a proxy for the concentration of suspended particles. The observations clearly identify thermal and b_{bp} intrusions down to ~700-800 m in the Bosporus inflow area. In this area, b_{bp} is more than five times larger than elsewhere, which could indicate bacterial abundance and possible biological involvement in the precipitation of Mn-containing particles. The b_{bp} anomalies become much shallower than the temperature anomalies with increasing distance to the east of the strait. Their maxima are located between the onset of the suboxic zone and the upper part of the anoxic layer. Unlike well-known intrusions that are caused by inflow, open-ocean intrusions are shallower and often characterized by multiple layers of backscatter maxima with thicknesses of only 15-20 m. The ratio between backscattering coefficients measured at two wavelengths, which gives a proxy for particle size, shows that the relative amount of larger-size particles in the anoxic layer increases with depth. The particle concentrations and their size distribution display different vertical variability, which indicates the complex transformation of biological matter. The lower concentration of particles and lower chlorophyll-a during the extremely warm 2016 reveals an overall positive correlation between the two properties. The trends in the particle backscattering coefficient in the suboxic zone during 2013-2016 could indirectly reveal a biogeochemical response to temperature changes.

Keywords:

Biooptical study of Black Sea

Biogeochemical response to intrusions

Particle size distribution

1 Introduction

The Black Sea is known as the largest anoxic basin in the world ocean, which has unique vertical chemical stratification [Konovalov et al., 2005] and where suspended particles play an important role in redox cycling [Lewis and Landing, 1991]. However, the temporal and spatial dynamics of particles and their link to these anoxic conditions have not yet been adequately sampled and remain poorly understood. This topic is of utmost importance because the dynamics of particles are strongly connected with the transformation of matter.

The Black Sea gives an excellent illustration of how important the physical processes are for the formation of biogeochemical states therefore we will first shortly introduce the dynamics of the Black Sea. This sea is an almost enclosed deep basin (mean and maximum depth 1,253 and 2,212 m, respectively) connected to the Sea of Marmara by the narrow Bosporus Strait. The difference between evaporation and precipitation is small to compensate for the fresh water excess due to rivers. Because of the narrow opening in the strait of Bosporus fresh water cannot be effectively exported, making the Black Sea a typical estuarine basin (its surface salinity is about half that of the Mediterranean).

The most specific characteristic of the Black Sea thermohaline fields is the distinct vertical density-layering, which tends to reduce the vertical exchange supporting a unique chemical and biological environment [Konovalov et al., 2005]. One consequence of the extremely stable stratification is the formation of cold intermediate water mass by winter cooling and the spreading of this water mass along isopycnic layers throughout

the sea. This cold intermediate layer (CIL) has a core at ~50 to 100 m below the surface. CIL is where the seasonal signal is well pronounced; its lower boundary decouples surface and deep waters.

Below the CIL temperature is rather uniform and density depends mostly on salinity, which increases down to about 300 m (bottom of halocline/pycnocline). In the deeper layers, the vertical gradient of salinity decreases slowly down to ~1600-1700m. Below this depth, vertical profiles of temperature and salinity are almost homogeneous.

The circulation in the Black Sea is structured usually in two connected cyclonic gyre systems encompassing the basin (the main current is known as the Rim Current). The cyclonical character of general circulation results in a dooming of pycnocline in the basin interior. Between the Rim Current, an essentially narrow jet current, and the coast a number of coastal anticyclonic eddies occur. For a short overview of the Black Sea dynamics, see Stanev (2005). The specific role of general circulation and coastal anticyclonic eddies for the Black Sea biogeochemistry and the ventilation of its anoxic waters is explained by Stanev (2014), who used dedicated numerical experiments.

The oxycline (chemocline) is known as the major transition feature between oxic and anoxic conditions, where the oxygen concentrations decrease by more than 200 μM in a less than 40-m-thick layer. The fine details of chemical stratification were described by Shaffer [1986] and Murray et al. [1989; 1995]. The suboxic zone, which is a transition layer between the oxic and anoxic domains, occurs in the halocline, where the oxygen and hydrogen sulfide concentrations are below the detection limits [Murray et al., 1989; 1995]. This zone shows very complex dynamics, which are not fully aligned to the thermohaline fields [Konovalov and Murray, 2001; Stanev et al., 2014].

Multiple layers of biological activity are observed in the Black Sea, including oxygenic and anoxygenic photosynthesis, chemoautotrophy, chemolithotrophy and heterotrophy [Jannasch et al., 1991; Jørgensen et al., 1991; Yılmaz et al., 1998; 2006; Wakeham et al., 2007]. According to Karl and Knauer [1991] photoautotrophic production in the Black Sea is restricted to the upper ~50 m of the water column, with values ranging between 0.7 and 15 mgC m^{-3} day^{-1} (see also Yilmaz et al. [2006]). Primary production is several times higher on the northwestern shelf area, where riverine discharges of nutrients are present [Cociasu et al., 1997]. The bacterial production rates beneath the euphotic zone and across the oxic-anoxic boundary are ≤6 mg C m^{-3} day^{-1} [Karl and Knauer [1991], indicating the rapid recycling of particulate organic matter in the suboxic zone compared to the relatively low rates of decomposition in the permanently anoxic zone. If the downward flux of particulate organic matter is unusually high or if deep water ventilation is restricted, bacterial metabolism can consume all the available oxygen [Karl and Knauer, 1991]. For primary and chemosynthetic production rates, see the data in Yilmaz et al. [1998; 2006].

The downward flux of particulate organic matter from surface waters is crucially important to maintain the present-day anoxic conditions of the Black Sea, motivating deeper analysis of particle composition and its dynamics. This subject includes both the coastal-open ocean exchange (which dominates matter production and export in the coastal zone) and the biological processes and sinking in the interior basin (which sustain export from the euphotic zone beyond the shelf-break). However, past observations have revealed many limitations in addressing the

complexity of the Black Sea's dynamics and biogeochemistry in a continuous manner with sufficient resolution. Thus, new robotic observations, such as the Biogeochemical-Argo floats (hereafter referred as BGC-Argo floats), represent an opportunity to investigate the complexity of the physical – biogeochemical coupling in this peculiar environment, with a specific focus on suspended particles (abundance and size distribution).

BGC-Argo floats are free-drifting Argo profilers that measure temperature and salinity and can carry additional sensors, such as oxygen optodes or optical sensors, to measure the chlorophyll-a (*Chla*) concentration, colored dissolved organic matter (*CDOM*) fluorescence, the backscattering coefficient, the beam attenuation coefficient, and downwelling irradiance [Boss et al., 2008; Bishop and Wood, 2009; Xing et al., 2012; Mignot et al., 2014; Xing et al., 2014, Organelli et al., 2016]. The aim of the so-called Biogeochemical-Argo program [Johnson and Claustre, 2016] is to monitor the global ocean over the long term to better understand and quantify important biogeochemical processes [e.g., Gruber, 2011; Johnson et al., 2009; Körtzinger et al., 2009; Claustre et al., 2010; International Ocean-Color Coordinating Group (IOCCG), 2011]. Here, we focus on BGC-Argo data that were acquired in one very specific ocean area, the Black Sea, where the state of the biogeochemical system differs largely from that of oceanic systems.

The processes in regional basins do not always match those that are observed in the world ocean, and knowledge from the oceanic BGC-Argo program is not easily applicable. Therefore, we must develop new biogeochemical observations in the Black Sea, with new techniques that are tailored to the regional conditions. This approach can improve our understanding of the spatial and temporal variations in some key biogeochemical variables, including the suspended particle concentration and size distribution, which are largely unknown because of the limited amount of appropriate observations. The sinking and decomposition of particulate organic matter are the main constraints on the ocean biological pump; currently, these factors are poorly understood and crudely represented in biogeochemical models. The particle size and density control the particle sinking rate and hence carbon export, but they are also altered by biological decomposition rates [Vries et al., 2014]. These processes are also very important for the strongly layered Black Sea system, where matter transformation is shaped by a complex interplay between the vertical fluxes of sinking particulate matter and the three-dimensional circulation and inflows from the Bosporus Straits.

In recent years, several profiling floats with oxygen sensors have been deployed in the Black Sea, which substantially advanced our understanding of the area's hydrodynamics and oxygen dynamics [Stanev et al., 2013; 2014]. What has not been addressed in these studies is the fine vertical layering of oxygen and some biogeochemical properties. One basic motivation for this investigation is to appropriately sample (in time and space) these waters to optimally resolve and explain the dominant variability of the area's physical and biogeochemical fields.

Our aim is to demonstrate that the limitations in the current observation capabilities over larger areas and long times can be overcome by using BGC-Argo profilers to advance our understanding of optical variability and related biogeochemical processes. The long-term aim is to establish how BGC-Argo can improve our understanding of the environmental factors that are responsible for the distribution, abundance and diversity of matter and different microorganisms in the Black Sea's water column.

Specificities of the Black Sea's biogeochemical features are clearly identified by optical signatures of its water masses. Reduced light transmission at the pycnocline depth, which has indeed been reported many times [White et al., 1989; Tebo et al., 1991; Özsoy et al., 1993], could be related to the abundance of suspended particulate Mn. These observations showed pronounced maxima that extended throughout the suboxic zone, with peaks near potential water densities of 14.7 and 16.1. Spencer and Brewer [1971] were the first to consider the vertical mixing and redox potentials as controls on the distribution of manganese and other trace metals.

Tebo [1991] observed a narrow particulate Mn maximum that was associated with extremely high potential bacterial Mn oxidation rates at water densities of 15.8-16.1. Thus, MnO_2 can serve as an oxidant for H_2S after dissolved Mn^{2+} is oxidized to particulate Mn(III,IV) above the anoxic layer and sinks back into the sulfidic zone [Tebo, 1991]. Lewis and Landing [1991] claimed that a light scattering layer near the sulfide interface was more likely caused by high bacterial abundances, with higher intensity near the coast because of more vigorous redox cycling. One additional objective of our study is to identify the location of particulate maxima with respect to key reference isopycnals by using continuous and high resolution measurements.

The slope that characterizes the spectral dependency of the backscattering coefficient $b_{bp}(\lambda)$ can be considered an indicator of the particle size distribution [e.g., Loisel et al., 2006; Kostadinov et al., 2009]; the steeper the spectral dependency, the greater the proportion of small particles. In the context of this study, measuring this slope will enable us to address changes in the relative concentration of small *vs.* large particles. The fine particle layer in the Black Sea, which is a feature of the chemocline between anaerobic and aerobic water, was first discovered by Brewer and Spenser [1974]. In our study, we demonstrate that the high-resolution BGC-Argo observations can detect and monitor this layer and describe its temporal and spatial variability and the close dependence of biogeochemical fields on physical fields.

The present work uses observations from two BGC-Argo floats that were equipped with multiple sensors (oxygen optodes, chlorophyll fluorometers, and backscattering sensors at 532 and 700 nm) and deployed in December 2013 in the western region of the Black Sea. This setup enabled us to simultaneously measure several biogeochemical and bio-optical properties [not only oxygen, as described by Stanev et al., 2013; 2014] in large areas of this sea (coastal ocean and open-ocean) over almost three years. We analyze the spatial and temporal variability of the thermohaline fields and oxygen, with a focus on the exchange between the coastal and open ocean. The relationships between different bio-optical properties, their dependence on hydrographic conditions and the dominant temporal and spatial evolutions are also addressed. Compared to our earlier research, this study's novelty is an analysis of the temporal and spatial variability of the *Chla* concentration ([Chla]), $b_{bp}(532)$ and $b_{bp}(700)$, which were sampled with very high vertical resolution, and the interrelationships among these properties.

This paper is structured as follows. We describe the materials and methods in section 2, followed by data analysis in section 3 and conclusions in section 4.

2 Materials and Methods

2.1 Observations

In the winter of 2013, two new Provor BIO biogeochemical floats were deployed and tested in the Black Sea. The first (WMO-7900591) was deployed on 16-Dec-2013 at 43.25 N and 29.25 E. This device performed 134 cycles before 18-Aug-2016, which is the last time in the analysis that is presented here. The second (WMO-7900592) was deployed on 15-Dec-2013 at 42.24 N and 29.00 E. This device performed 79 cycles and terminated its mission on 26-Oct-2014. These profiling floats used iridium transmissions and a sensor suite that consisted of pressure, temperature, and salinity sensors; an Aaanderaa optode to measure dissolved oxygen; two calibrated fluorometers to measure the chlorophyll concentration; a backscattering sensor to measure the particle backscattering coefficient; and a sensor to measure the downward radiation. The maximum profile depth was set to

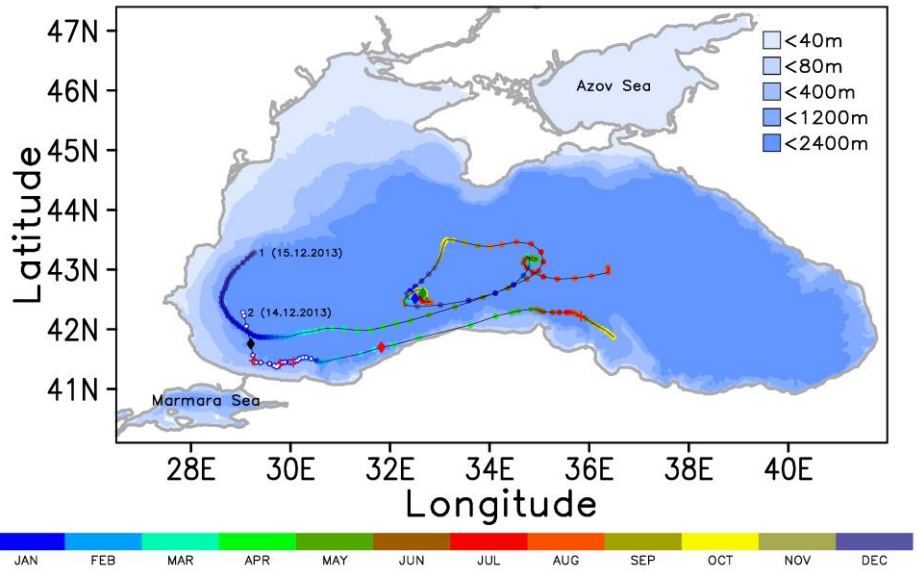

Figure 1. Trajectories (black lines) of the floats WMO-7900591 (1 in the figure) and WMO-7900592 (2 in the figure). The dots identify the surfacing position, and their colors are specified to approximately represent seasonal changes in the SST, which can be easily translated into time (color bar). This coarse presentation of the "timing" is used to avoid numbering all the surface positions and to display the chronology of the observations. The launching positions and times are also provided. The small white dots on the surface positions of WMO-7900592 (white dots with blue outlines) identify portions of the trajectory for which more detailed analysis is provided in the text. The diamond symbols identify the positions, time (in addition to the day after 1-Jan-2014) and profile number on the trajectories, which are mentioned in the text. WMO-7900591: diamond (blue), 16-Mar-2015; diamond (green), 15-May-2015; WMO-7900592: diamond (black), 22-Dec-2013; diamond (red), 23-Mar-2014. Four coordinates along

the trajectory of float WMO-7900592 have been marked by "+" to identify its positions on 30-Dec-2013, 13-Jan-2014, 20-Jan-2014, and 05-Sep-2014 where data are discussed further in the text.

1000 m. Sampling by WMO-7900591 was performed daily until 16-Jan-2014, every fifth day between 28-Jan-2014 and 11-Apr-2014, and once every 10 days afterwards. The corresponding changes from fine temporal sampling at the beginning to coarser sampling during the second phase of mission of WMO-7900592 were done at 28-Jan-2014 and 08-Apr-2014. More technical details of this measuring process can be found at http://www.ifremer.fr/co-argoFloats/float?ptfCode=7900591 and http://www.ifremer.fr/co-argoFloats/float?ptfCode=7900592.

The trajectories of both floats (Fig. 1) show that WMO-7900591 mostly operated in the deeper portion of the Black Sea, while WMO-7900592 first moved into the area of the Bosporus Straits and then followed the coast. These different trajectories for the two floats provide an excellent opportunity to analyze the differences between deep-ocean and coastal-ocean biogeochemistry. A similar exercise for only oxygen and with coarser vertical resolution was previously presented by Stanev et al. [2013; 2014].

2.2 Methods

Argo observations in the Black Sea were previously analyzed by Korotaev et al. [2006] and Stanev et al. [2013, 2014], so we will refer to these publications for further methodological details. In the following, we only present the methods that were used to obtain biogeochemical data from the profiling floats, which has not yet been considered in the Black Sea literature. First, sensor biofouling is not an issue in the Black Sea. In addition to natural protection from the float mission's configuration (most of the (drift) time passed in the dark and at low temperature plus regular drastic changes in pressure), the anaerobic conditions of the Black Sea represent a mechanism of protection. A "natural calibration" with respect to oxygen occurs in the Black Sea every time a float produces a new profile because a "solid zero" exists at depth. Our analysis of data from the anoxic layers never showed oxygen values that were higher than 1 μM, which can roughly be considered an error estimate for the analyses in this paper. No calibrations of optode others than provided by manufacturer has been made.

An additional step in this study compared to earlier BGC-Argo observations is the very fine vertical resolution that was specified for some sensors and depth intervals. The vertical sampling rate of the CTD (temperature and salinity pressure) and oxygen sensors in the two floats was set to 1 dbar. For *Chla*, $b_{bp}(532)$ and $b_{bp}(700)$ this fine vertical sampling was applied only for the first 250 m, which is deep enough to resolve the basic elements of the Black Sea's biogeochemical stratification. Below this depth, the vertical sampling was coarser. After 17-Oct-2014, the zone of fine vertical sampling was extended to 350 db for WMO-7900591.

2.2.1 Light scattering

The particle scattering coefficient, $bp(\lambda)$, is considered as first-order proxy of the suspended particle mass concentration in the size range between sub-microscopic particles and ~10 μm. The backscattering coefficient, $b_{bp}(\lambda)$, corresponds to the portion (~1-3%) of the scattering coefficient that is scattered towards the backward

direction. As bp(λ), b_{bp} (λ) is primarily driven by suspended particle mass concentration (e.g. Lorthiois et al. [2012]), and is dependent to the second order on the particle composition (through they refractive index) and the particle size distribution (PSD) (e.g. [Morel and Ahn, 1991; Stramski and Kiefer, 1991]). Fine particles are potentially the most efficient in terms of light backscattering because of their potentially higher refractive index. These particles include small, non-living particles and heterotrophic bacteria [Morel and Ahn, 1991; Stramski and Kiefer, 1991] as well as coccoliths [Balch et al., 2001]. Backscattering sensors are more sensitive to fine particles with high refractive index (e.g. bacteria, coccoliths, mineral particles). The corollary is they are rather insensitive to large aggregates of the marine snow type or fecal pellets.

The occurrence of a high-turbidity nepheloid layer (Rozanov et al., 1998] can likely be recorded in the b_{bp}(770) (Lorthiois et al. [2012]).Therefore backscattering measurements are potentially well-tailored to the Black Sea's conditions, which are characterized by abundant heterotrophic bacteria and is also is largely dominated by river runoff.

The Wetlabs ECO Triplet Puck sensor that was used in this study measures the volume scattering coefficient (m^{-1} sr^{-1}) at 124° and for two wavelengths: 532 nm and 700 nm. These measurements were subsequently converted into $b_{bp}(532)$ and $b_{bp}(700)$ by using the methodology that was initially described in Boss and Pegau [2001] and adapted for BGC-Argo data management by Schmechtig et al. [2015] for any wavelength, λ:

$$b_{bp}(\lambda)=2*\pi*1.076*[(\beta_b(\lambda)-D_{bb}(\lambda))*S_{bb}(\lambda)-\beta_{sw}(\lambda)],$$

where b_{bp} (λ), m^{-1}, corresponds to the particle backscattering coefficient; $\beta_b(\lambda)$ is the raw count for the sample of interest; $D_{bb}(\lambda)$ is the dark count of the sensor; $S_{bb}(\lambda)$ is the scaling factor in m^{-1} sr^{-1} $count^{-1}$; and $\beta_{sw}(\lambda)$ is the contribution to the volume scattering function by pure seawater in m^{-1} sr^{-1}. The factor of conversion 1.076 for 124° was determined by Sullivan et al. [2009]. No further data quality control or treatment was applied to the backscattering data.

The spectral dependency of the backscattering coefficient has been proposed as a proxy for the relative particle size distribution [Loisel et al., 2004; Kostadinov et al., 2009]. High values of the spectral dependency are characteristic of a higher proportion of small particles with respect to larger ones. Reciprocally, lower values are characteristic of a lower proportion of these small particles with respect to larger ones. Here we used the two channels (532 and 700 nm) of the Wetlabs sensor to estimate the spectral dependency of the particulate backscattering, The ratio of the relative concentrations of small vs. large particles, which is a measure of this spectral dependency, increases with increasing b_{bp}(532)/ b_{bp}(700). For of brevity, we will hereafter call this qualitative index the S-index ("S" stands for "size").

Analysis of time series of b_{bp}(532) and b_{bp}(700) when floats were parking at 1000 m, and where the optical signal are expected to be stable over time, reveals that b_{bp}(532) start to decrease for float WMO-7900591 after ~1 year of operation. This is possibly due to aging green LED. Therefore, the time series of S for both floats can accurately be used only over the first year of acquisition. For float WMO-7900591 and for the remaining period of its acquisition for this float, only the relative vertical distribution of S-index can be analyzed for each profile.

At present, it is not possible to define the thresholds for a dominance of small versus large particles (e. g., a large particle-size, a small particle-size, and a medium particle size). Therefore S-index is considered here only as a relative indicator of temporal-spatial change of large versus fine particles in the size range 0-10 μm. Finally, we remind that backscattering sensors measure optical properties, from which it is not straightforward to deduce the particle types. Therefore they can only indirectly describe the biogeochemical properties.

2.2.2 Chlorophyll

The concentration of *Chla*, [Chla] (mg m^{-3}), was retrieved from the chlorophyll fluorescence sensor (Ex/Em at 470/695 nm) of the Wetlabs ECO Triplet Puck. The [Chla] retrieval equation can be written as follows (Schmechtig et al., 2015b]:

$$[Chla]=(F_{Chla} - D_{Chla})*S_{Chla,}$$

where F_{Chla} is the raw count of the sample of interest, D_{Chla} is the dark count of the sensor, and S_{Chla} is the scaling factor in mg Chla m^{-3} $count^{-1}$. There were no possibilities to take water samples during the deployment and compare bio-optical estimates with collected samples.

The examination of the Chla fluorescence profile revealed a steady increase in the signal with depth in the anoxic layer, which was obviously not caused by a true increase in [Chla]. This feature was instead interpreted as an increase in the concentration of some fluorophores, whose excitation/emission characteristics overlap those of *Chla*. Röttgers and Koch [2012] recently noted the possible contribution of porphyrin by-products, which could explain this apparent increase in *Chla* fluorescence, particularly in the oxygen minimum zone of the tropical ocean.

The [Chla] value was set to zero in the anoxic waters because of this *Chla* fluorescence contamination and by assuming [Chla] should be zero. Following this correction step, a quenching correction procedure, which was introduced by Xing et al. [2012], was used to remove the influence of non-photochemical quenching on the fluorescence signal at the surface, as described in Schmechtig et al. [2014].

3 Data analysis

3.1 Deep-water intrusions

The physical variables (temperature, salinity and density) that were observed by WMO-7900591 and WMO-7900592 revealed features of vertical stratification, which are well known from earlier observations [including Argo floats; Stanev et al., 2013]. The time versus depth diagram of temperature and $b_{bp}(532)$ below the upper layer (Fig. 2a, b) is analyzed to check the correlations between the physical and biogeochemical parameters, which could identify common penetration pathways. On 26-Dec-2013, when the float WMO-7900592 reached the position that is denoted by the black diamond symbol in Fig. 1, the sensors recorded a jump in temperature and $b_{bp}(532)$; the signal penetrated below 700 m, supporting earlier evidence for penetration deeper than 700 m that was

provided by Murray et al. [1991]. This drastic change appeared in the area of the Bosporus Straits, so the float likely detected a mixture of Marmara Sea and Black Sea water, a *direct consequence* of the propagation of gravity currents onto the continental slope. Profiles with shallower $b_{bp}(532)$ maxima could result from shallower slope current intrusions or open-ocean processes (see section 3.4).

The coincidence between the temperature and $b_{bp}(532)$ anomalies indicates a common source of materials that can be traced back to the Bosporus Straits area [Codispoti et al., 1991; Özsoy et al., 1993]. In the past, the mixing between Bosporus inflow and Black Sea water was very difficult to observe [Latif et al., 1991; Gregg and Ozsoy, 1999; Ozsoy et al., 2001]. Cruises have attempted to trace this flow and associated mixing. Coarse resolution or inappropriate parameterizations in numerically simulations [Stanev et al., 2001; 2004, Ozsoy et al., 2001] prevented these authors from adequately resolving the thin bottom-attached plume, which intruded into the Black Sea at the appropriate density when reaching the shelf break. The black diamond in Fig. 1 illustrates the limits beyond which bottom-arrested flows did not penetrate. As seen in the records from the float WMO-7900591, deep intrusions to the NW of this point did not occur.

The intermediate temperature maximum (this layer has been first documented by Murray et al. [1991]), evolved into patchy structures but persisted at approximately 500-m depth for longer than one month with increasing distance from the strait (see the trajectory in Fig. 1). The depth of the cores of the $b_{bp}(532)$ and temperature maxima were comparable at the positions of the intrusions, and this pattern remained over the next five days. However, the $b_{bp}(532)$ subsurface maximum eventually became shallower than the temperature maximum, which indicates that their evolution was controlled by different processes, although the origin of the temperature and $b_{bp}(532)$ maxima was likely the same. While physical processes (e. g. along-isopycnal propagation of anomalies originating from the strait) can explain the almost constant position of intermediate temperature maximum, the upward displacement of the $b_{bp}(532)$ core needs further consideration (see next sections).

3.2 Temporal variability of the hydrophysical fields

Fig. 3 which presents time versus depth diagrams of the temperature, salinity and depth of isopycnal surfaces helps us understand the physical control on the temporal variability of the biogeochemical properties. The evolution of the CIL, as seen in the changes in the positions and shapes of the 8.25, 8.5 and 8.75 °C isolines (Fig. 3a), shows good persistence over most of the time and in the observed areas. The CIL had eroded in some locations (see the event around 5-Jul-2015). The change in the temperature profiles between 2013 and the extremely warm 2016 demonstrates that no intermediate water was cooler than 8.75°C by the fall of 2016. Obviously, the CIL is warmer than it has been for several decades [Blatov et al., 1984, Oguz et al., 2006]. Our observations support earlier analyses by Stanev et al. [2013], who indicated that cooler temperatures than 8°C were rarely observed in the core of the CIL, which suggests a warming of approximately 1°C in the CIL over the past 3-4 decades.

The temporal evolution of the salinity (Fig. 3b) almost matches the evolution of the density below 50 m (see the depth of the isopycnal surfaces in Fig. 3c) because the salinity most prominently controls the evolution of the density in the deeper layers. The seasonal thermocline can be clearly seen in the evolution of the density field,

which demonstrates that the temperature was the dominant field in the surface layer (the contribution of salinity to density changes is smaller there).

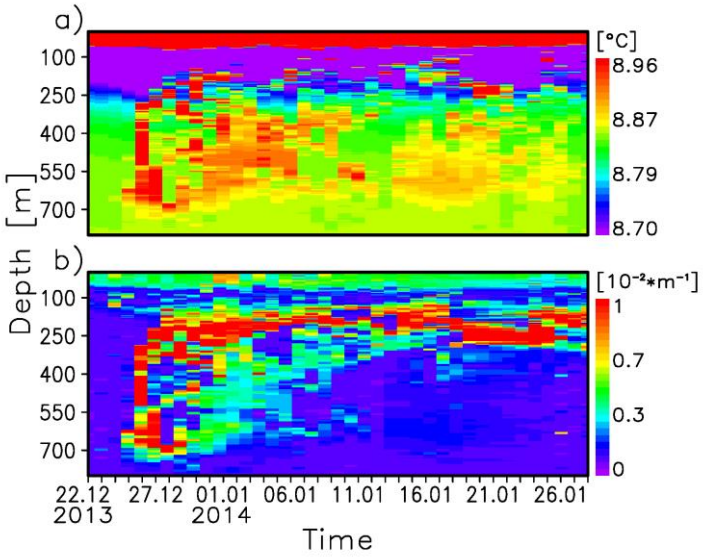

Figure 2. Depth versus time profiles of the temperature (a) and $b_{bp}(532)$ (b) that were measured by WMO-7900592. The diagram shows data for only one portion of the trajectory (Fig. 1), with the small dots in the middle of the larger dots (in color) showing the surface positions. The black diamond along the trajectory is for 26-Dec- and identifies an outbreak of particle concentrations and positive temperature anomalies. The time of this outbreak is identified in the figures by the time of first appearance of higher temperature over depth interval of more than 300 m.

Two interesting events were recorded by WMO-7900591: one on 24-Mar-2014 and one on 5-Jul-2015. The first event occurred during the period of cold water formation, which was accompanied by a change in the salinity and contributed to pumping cold waters into the CIL. The second event, which appeared in the summer, was the reason behind the erosion of the CIL.

WMO-7900592 which followed the southern coast showed deep penetrating signals that originated from the surface close to the Bosporus Strait (between 23- Dec-2013 and 1-Feb-2014). This period coincides with extreme cooling and cold water formation, which explains the massive intrusions of oxygen-rich waters down to 150 m (see later in the text). During January-February 2014, both BGC-Argo floats were in the southwestern Black Sea and likely experienced similar atmospheric conditions. However, WMO-7900591 was in the open sea, while WMO-7900592 was closer to the coast. Both floats registered cold water mass formation, but this process was more pronounced closer to the southern coast compared to the basin interior.

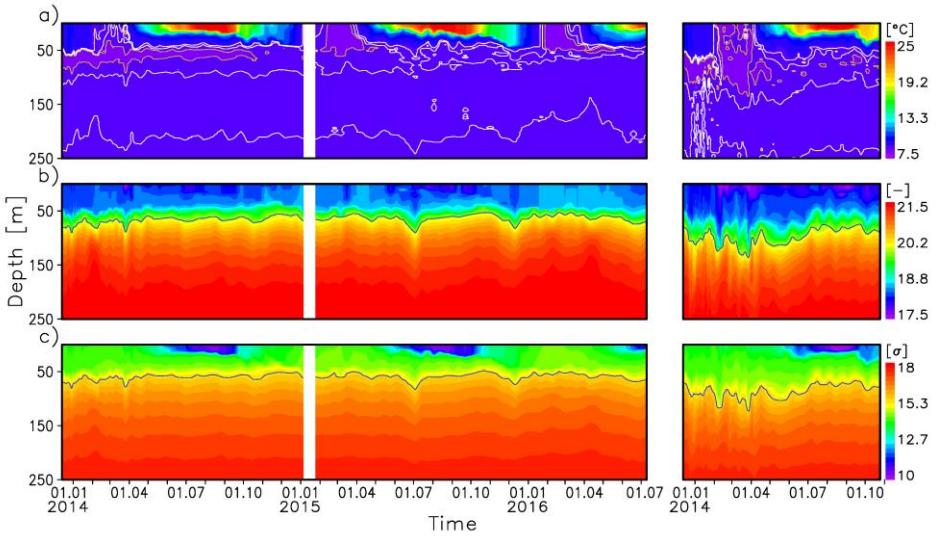

Figure 3. Time versus depth diagrams of the temperature (a), salinity (b) and density (c). The longer-time diagram (left) is from WMO-7900591, and the shorter diagram (right) is from WMO-7900592; the latter terminated earlier its operation. Additional isolines were plotted to more clearly present the temporal evolution in zones where the color resolution is insufficient: 8.25, 8.5, and 8.75 °C for the temperature; 19.9 for the salinity, which is approximately the bottom of the CIL; and 1015.5 kg/m^3 for the density, which is also approximately the bottom of the CIL. The outcropping isolines that are plotted with red (8.25°C) approximately illustrate the location and timing of cold water formation.

Such data records were almost impossible in the past, when ship-based observations were used (very few such observations have been recorded in the winter season).

3.3 Temporal variability of biogeochemical fields in the upper layer

Biological systems actively respond to changes in thermohaline fields. This concept is true in the upper mixed layer, where the heat and oxygen fluxes that are associated with air-sea interactions, along with the light availability and nutrient supply, shape the temporal and spatial evolution of biogeochemical properties. Of utmost importance for the following discussion are the consequences of changing water column stability and resulting intrusions. Time series of oxygen, *Chla* and $b_{bp}(532)$ are shown in Fig. 4 from the surface down to 250 m because most of the variability of biogeochemical fields occurs in this layer. The major characteristic of the vertical distribution of *Chla* is its subsurface maximum in the summer, when phytoplankton grows closer to the nitracline (if light penetrates sufficiently deeper). It is known that in the open ocean *Chla* and $b_{bp}(532)$ do not perfectly co-vary because of photoacclimation. In the Black Sea this correlation is even weaker.

Previous observations in the world-ocean [e. g., Anderson, 1969] and analysis of BGC-Argo data [Stanev et al., 2014] demonstrated that the subsurface oxygen maximum in the summer was caused by photosynthesis in the photic layer. Our observations support these findings: an increase in [*Chla*] was followed by changes in the oxygen concentration, thus indicating increased oxygen production. The subsurface oxygen maximum is more evident in Fig. 5a because the temporal variability in the strongly stratified upper layers is better resolved when presented in density coordinates. A comparison between Fig. 5a (oxygen) and Fig. 5b ([Chla]) demonstrates that their patterns show a different structure, although the subsurface maximum is dominant for the both fields.

The subsurface [Chla] maximum at ~30 m follows spring-summer re-stratification, which began on approximately 23-Mar-2014 and 18-Mar-2015. This feature appeared after the formation of the CIL (compare Figs. 3 and 4). Afterwards, a clear [Chla] maximum was observed. This maximum originated from the surface layers (less pronounced in the record of WMO-7900591 during the first year). The very weak winter convection in 2016 may explain the lower [Chla]. However, the subsurface maximum could also be clearly seen during this year, which is not the case for oxygen because of the very high surface temperatures.

This observed evolution of the upper-ocean [Chla] and oxygen is reminiscent of ocean spring blooms followed by the establishment of a subsurface maximum, thus revealing the propagation of the signal from the spring bloom into the deeper layers. The weak surface maximum and the well-pronounced subsurface maximum during the first year that were recorded by the float WMO-7900591 would suggest either that it could be measuring a later state of the blooming period or that the [Chla] maximum had an advective nature in some areas. The high concentrations of the subsurface [Chla] maximum persisted until the late summer, while the [Chla] in the surface layer remained small, which is consistent with earlier analyses and interpretations [Yılmaz et al., 1998; Konovalov et al., 2006;Yakushev et al., 2007; Grégoire and Soetart, 2010; Stanev et al., 2014]. Notably, the multi-layer structure of *Chla* in the summer can be better seen when data are represented in isopycnic coordinates (Fig. 5b). Below the upper mixed layer, the [Chla] continuously decreased to almost zero at the depth of the suboxic zone.

The vertical white strips identify times when the data quality was poor. Additional isolines were plotted for the oxygen to more clearly present the temporal evolution in zones where the color resolution is insufficient: 5 µM (red) and 50 µM (white). These isolines are repeated in some other plots to facilitate the identification of similarities and differences in the temporal evolution of different variables in the areas around the suboxic zone. The Chla diagrams are plotted down to the upper boundary of the suboxic zone (see the explanation in section 2).

The backscattering coefficient data distinguish a surface layer with high $b_{bp}(532)$ values and a second maximum in the deep (anoxic) layers. The data for *bbp(700)*, which are not presented here, show similar temporal-spatial characteristics as in the $b_{bp}(532)$ profiles, which demonstrates that particles with different sizes undergo similar evolution. This decoupling of b_{bp} layers would suggest that particles from the upper layers do not sink below the upper boundary of suboxic zone and that particles in the suboxic zone are generated there.

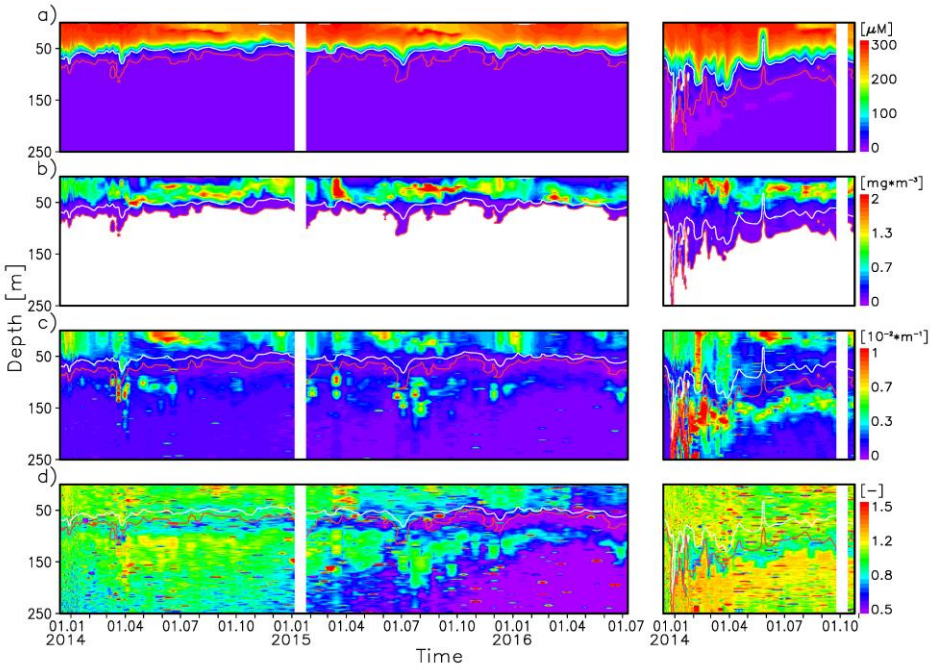

Figure 4. Time versus depth diagrams of oxygen (a), [Chla] (b), b_{bp}(532) (c) and the ratio of b_{bp}(532) versus b_{bp}(700) (d). The vertical white strips identify times when the data quality was poor. Additional isolines were plotted for the oxygen to more clearly present the temporal evolution in zones where the color resolution is insufficient: 5 μM (red) and 50 μM (white). These isolines are repeated in some other plots to facilitate the identification of similarities and differences in the temporal evolution of different variables in the areas around the suboxic zone. The Chla diagrams are plotted down to the upper boundary of the suboxic zone (see the explanation in section 2).

Although $b_{bp}(532)$ has a clear maximum in the surface layers, this factor shows a much patchier distribution compared to oxygen. The comparison of $b_{bp}(532)$ with the *Chla* data does not show identical patterns (compare Fig. 5c with Fig. 5b), which indicates that the correlation between [Chla] and $b_{bp}(532)$ is much weaker in the Black Sea compared to some open-ocean areas [Loisel et al., 1998; Huot et al., 2008]. In open-ocean waters, the particulate backscattering coefficient is mostly driven by phytoplankton or its biogenic by-products. Here, the weak co-variation of the backscattering coefficient with [Chla] likely reveals the specificities that are associated with the estuarine nature of the Black Sea.

The position of oxygen isoline 5 μM (red line) is close to the upper boundary of the suboxic zone and, in the absence of sulfide measurements, approximately identifies the position of the upper layers of anoxic zone (about 50 m below the upper boundary of the suboxic zone). $b_{bp}(532)$ shows clear signatures of deep particle penetration, mostly from the upper portion of the anoxic zone, which is better pronounced in the observations from WMO-

7900592. Here we remember that we detected and discarded some of the deep fluorescence signal in anoxic waters. There is a possibility that this signal could indeed have measuring settling phytoplankton cells. The combinations between fluorescence and backscattering in the deeper water layers might tell us about the origin of the particles

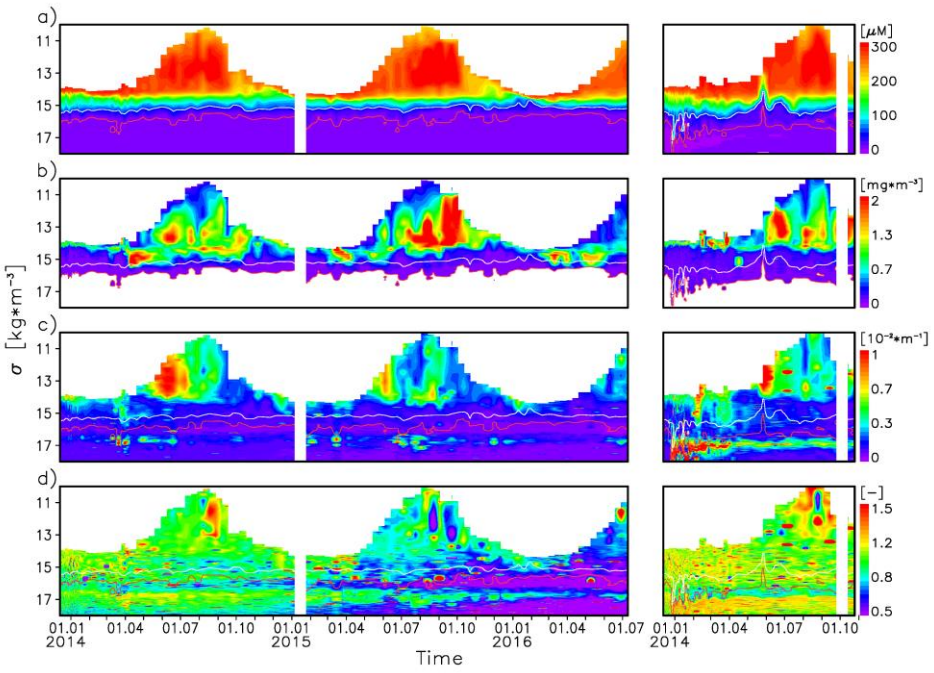

Figure 5. Same as in Fig. 4, but plotted against density.

detected at depth. However, interpretations in this direction need further direct (not only optical) observations and deeper analysis.

Some very important differences in the variability that were registered by the two floats, similar to the thermohaline characteristics, are noteworthy. During the period of extreme cooling, the upper (well oxygenated) layer became much thicker in the coastal zone (compare the left and right sides of Fig. 4a), and massive intrusions of oxygen-rich waters below 250 m were observed by WMO-7900592. This feature was accompanied by an increase in the thickness of the zone, with a high level of backscattering (see the right side of Fig. 4c).

3.4 Biogeochemical variability in the main pycnocline

3.4.1 Temporal and spatial variability

The position of the oxycline is approximately displayed in Fig. 4 by the 5 µM (red) and 50 µM (white) isolines. The thickness of the layer between these isolines is approximately 25 m in the open ocean and

approximately 40 m in the coastal zone. This thickness varies mostly because of changes in the thermohaline stratification. Fig. 4 clearly shows that both isolines that bound the oxycline are not exactly parallel, which indicates short-time temporal-spatial variability. Additionally, the depth of the oxycline (in geometrical coordinates) is shallower in the open ocean.

The backscattering coefficient $b_{bp}(532)$ shows a minimum at the depth of the red isoline in Fig. 4c, which is at the base of the oxycline. This backscattering-minimum zone, which is also well pronounced in density coordinates, with its axis at approximately σ_t=15.7 (σ~16.1) in the open sea and σ_t=15.9 (σ~16.4) along the southern coast (Fig. 5c), extends over the suboxic zone. The variability of the $b_{bp}(532)$-minimum zone as recorded by WMO-7900592, particularly when the float was close to the Bosporus Straits, is very noisy. The basic message here is that the oxycline decouples the upper and deep $b_{bp}(532)$-maximum zones.

The most important feature in the deep-water biogeochemistry that was detected from the BGC-Argo floats is the backscattering-maximum in the upper portion of the anoxic layer, which is very clear as seen in the observations from WMO-7900592. WMO-7900591 also revealed a similar signal, albeit weaker and patchier. The increased particle abundances near the coast according to these observations could be explained by the more vigorous redox cycling at this location [Lewis and Landing, 1991]. The largest $b_{bp}(532)$ values recorded by WMO-7900592 were near the Bosporus Straits (between 01-Jan-2014 and 11-Apr-2014 in Figs. 4 and 5).

During the first days after deployment, both floats measured very similar backscattering coefficient profiles (low backscattering was also measured by WMO-7900592) because they were following approximately the same water mass. The records of WMO-7900592 changed drastically when it entered the area of the Bosporus Straits' inflow (see Fig. 2). This observation clearly suggests that the backscattering maximum originated from this location and propagated over the entire sea. The maximum in the coastal area was below the sea surface. This result, together with the deep backscattering maximum being decoupled from the surface maximum, indicates that the origin of the deep backscattering was likely associated with gravity currents from the straits, which penetrated deeper than 150 m and sometimes deeper than 250 m.

3.4.2 Particle size distribution index

As mentioned in section 2.2.1, the *S*-index, which is presented as $b_{bp}(532)/ b_{bp}(700)$, quantifies the ratio between the concentrations of small *vs.* large particles. Although $b_{bp}(700)$ shows qualitatively similar patterns as $b_{bp}(532)$ within the first order, some nuances do exist between both measurements. Indeed, the S-index presents some temporal and vertical dynamics that can be tentatively interpreted as changes in the nature of particles, particularly their size distribution (Figs. 4d and 5d). The basic spatial variability in the S-index revealed an increase in the surface and intermediate layers and a decrease in the suboxic zone. These results suggest that the particle size distribution in the suboxic zone changed so that larger particles dominated the layer around σ_t =15.7 (open sea) and σ_t =16 (along the southern coast). The S-index increased rapidly with increasing depth, reaching a maximum at σ_t =16.1 in the open sea and σ_t =16.2 (along the southern coast). These changes could have been caused by the increasing abundance of particulate matter from the manganese transformation cycle and bacterial activity [see Tebo, 1991; Morgan et al., 2006].

The lower boundary of the oxycline decoupled the surface and deep layers, which are characterized by large particulate matter content; the abundance of large particles changed very significantly within the same zone. The representation in density coordinates reduced the noisiness of the signals and clearly demonstrated that the low-turbidity layer (Fig. 5c) overlaps (at least partially) layer of minimum S-index (Fig. 5d). These conclusions are even better illustrated in the scatter-plots in Fig. 6, which reveal a clear S-shape for this index, consistent with the observations of Morgan et al. [2006]: (1) the dominance of larger particles (small S-index) in the upper portion of the suboxic zone, (2) a tendency of decreasing particle size in the deeper areas of the suboxic zone (the S-index reaches a maximum approximately where the particles' concentration is the highest), and (3) a slow increase in the relative amount of larger particles in the deeper layers.

The large turbidity, which is accompanied by a relative increase in the concentration of smaller particles in the lower portion of the suboxic layer and upper portion of the anoxic layer, is reminiscent of the results by Lewis and Landing [1991], who claimed that higher particulate Mn concentrations were observed at somewhat shallower depths than the transmission minimum. This result suggested that the light scattering layer is more likely caused by high bacterial abundances. Thus, our results could motivate the usage of BGC-Argo to map the temporal and spatial variability of heterotrophic bacteria.

Particle sorting shows a strong regional dependency, which is exemplified by the differences in the relative increase in the concentration of smaller particles in the upper portion of the anoxic layer. This phenomenon occurred at approximately 120 m in the basin interior and deeper in the area of the Bosporus Straits (150-200 m). The core of the $b_{bp}(532)/\ b_{bp}(700)$ maximum layer was located at σ=16.8 (σ_t=16.07) in the open sea and σ=16.7 (σ_t=16.25) in the coastal zone.

The seasonal signal did not reach the suboxic zone. However, some temporal or spatial evolution may still have occurred at these depths. As seen in the time series from the open-ocean float (WMO-7900591), which were continuously recorded over almost three years, the size distribution was subject to significant evolution. At the beginning of the observation period, the core of the fine-particle layer was very well pronounced (Fig. 4d). During this initial period, WMO-7900591 was not far from the straits area. Over the following half year, this float flowed parallel to WMO-7900592 before entering the basin interior. Because of this increasing distance from the strait, the $b_{bp}(532)/\ b_{bp}(700)$-maximum layer (at approximately 150 m) weakened, and the S-index revealed a larger particle assemblage on 16-Jul-2015. A substantial transformation occurred in the CIL during the same period (Fig. 3a), which was followed by changes in the depth of the isopycnal surfaces (Fig. 3c). Thus this change in particle size was associated with changes in the thermohaline fields around and below the CIL (see Fig. 6c, where the profiles between 16-May-2015 and 24-Jul-2015 are plotted with black symbols). Obviously, the particle size distribution index decreased for the entire water column down to approximately 400 m. A comparison between Figs. 6c and 6f and Fig. 6i demonstrates that the S-index was smaller in the open sea because the relative contribution of larger particles was more prominent. As seen in Fig. 5d, the float WMO-7900591 approached the southern coast again by 5-Jul-2015, which could explain the increase in the S-index. After its rapid movement to the east in the winter of 2016, this float "stagnated" again in the central Black Sea (north of Synop), where the $b_{bp}(532)$ and S-index

decreased again. No clear seasonality was observed along the axis of the maximum S-index in the upper area of the anoxic zone.

The S-index suggests that the biogeochemistry in the Black Sea experiences spatial sorting. This change in the S-index with increasing distance from the coast could reflect a changing proportion between small and large bacteria in different areas. The decrease in the S-index over the last three years could reflect the response of biological systems to less cold water in the CIL.

3.4.3 The backscattering coefficient as a proxy for particle concentration and size distriburion

The present BGC Argo observations cannot be directly compared to *in situ* biogeochemical observations because such do not exist for the times and positions of used profiles. Therefore in the following we will discuss the consistency of our bio-optical observations with previous *in situ* ones. Observational evidence that was provided by Morgan et al. [2006] indicated that the heterotrophic bacterial biomass in Sakarya Canyon was high. According to Yilmaz et al. [2006], the chemoautotrophic production at this location reached 1930 $mgCm^{-2}d^{-1}$, which was approximately 30 times higher than the value in the central gyre. However, our measurements cannot determine whether the gravity currents brought this particle-rich water mass from the strait or if $b_{bp}(532)$ increased as gravity currents mixed with the ambient water, causing the resulting matter transformation. A very low oxygen concentration in this area would indirectly favor the second hypothesis. As seen in Fig. 6g, oxygen intrusions were measured in the inflow area down to a density level of 18.30 (σ_t~16.85). This density level corresponds to a depth of 350 m and is much deeper than the estimate of Konovalov et al. [2003] who claimed that intrusions can be traced to depths with densities as large as σ_t=16.6 (200 m). Later, we more closely examine different intrusion regimes.

Representing data in density coordinates supports earlier analyses of the isopycnic nature of mixing governing biogeochemical parameters [Konovalov et al., 2005; Stanev et al., 2004]. As illustrated in Fig. 5c, the backscattering maximum occurred at approximately σ=16.75 (σ_t=16.15) in the open ocean and σ=16.9 (σ_t=16.25) in the coastal zone. While a stronger coastal maximum was very well consolidated around the respective isopycnal depth (Fig. 6e), the maximum in the open ocean (Fig. 6b) was noisier and showed an intermittent multilayer structure (Fig. 5c). These results find an indirect support in the analysis of Konovalov et al. [2003], who showed that the maximum concentration of particulate manganese was substantially higher in the southwestern area of the sea (notice the different $b_{bp}(532)$ axes in Figs. 6b and e and Fig. 6h).

The observed backscatter maxima could reflect either bacterial abundance or particles and aggregates that are associated with manganese cycling. Unfortunately, the bio-optical sensors that we used here cannot directly distinguish between bacteria and manganese-loaded particles. Thus, we refer to Tebo [1991]: “although there may be some relationship between particle concentration and the presence of particulate Mn around the interface, light scattering data should not be used as a measure of particulate Mn”. Light scattering also cannot identify specific bacteria types, so the biogeochemical interpretation of our observations requires a careful analysis in the future.

The explanation of abundance or particles as related to bacteria is supported by Yilmaz et al. [2006], who stated that chemoautotrophic production enhances the bacterial biomass and elemental cycling. Jorgensen et al. [1991] estimated the chemoautotrophic production to be equivalent to 10-32 % of the surface primary production.

The bacterial variables in the Black Sea (abundance, incorporation rates, biomass, production, and specific growth rates) in 2001 were studied by Morgan et al. [2006]. Their method identified sub-microscopic and ~10-µm particles alongside large, filamentous bacteria. The mean bacterial abundances were approximately 0.38 x10^9 cells l^{-1} in the oxycline. This study determined that large filamentous bacteria (>10 µm) were present below the suboxic boundary and comprised up to 10% of the total bacterial abundance and up to 53% of the total bacterial biomass. Particle-attached autotrophic denitrification by intrusions of the Bosporus Plume has been studied by Fuchsman et al (2012). They demonstrated that accounting for particulate manganese helps explain the bacterial data.

The explanation of abundance or particles as related to processes that are associated with manganese cycling matches the theory of Kempe et al. [1991], who suggested that the light-transmission minimum at σ_θ=16.1-16.4 was caused by Mn-containing particles. In this density range, manganese was always present in dominant quantities in the form of finely dispersed (ca. 0.5-µm diameter) microspherules. Data that were compiled by White et al. [1989] clearly demonstrated the negative correlation between light transmission and the particulate manganese concentration at a density level of 16.05-16.1 [see Fig. 6c in Tebo, 1991].

The $bp(\lambda)$ value serves as a proxy of the particle load in the sub-microscopic to ~10-µm range. However, some overlap could exist between the sizes of Mn-containing particles and bacteria. Furthermore, very large filamentous bacteria could remain un-sampled by the BGC-Argo sensors. Differentiating between Mn-containing particles and bacteria is also difficult because manganese cycling is biologically catalyzed and a biological role in Mn precipitation may be possible [Tebo, 1991]. Furthermore, biooptical measurements cannot identify whether biological transformation or physical aggregation/disaggregation is more important for the observed change; they just register the change.

In spite of above interpretation-problems, addressing the dynamics of particles and their size-evolution, as seen by the BGC-Argo, even with these caveats, can be considered an important new step. Our continuous observations clearly revealed that the particle size and particle abundance followed different vertical changes. The coincidence between the depths where the particle concentration and the contribution of smaller particles are the highest indirectly supports Fig. 4 in Yilmaz et al. [2006], who claimed that the chemoautotrophic production peaked at the lower boundary of the fine particle layer. As seen by the dispersion of the BGC-Argo data, this overall rule undergoes large temporal and spatial variability.

3.4.4 Appearances of intrusions

The large number of profiles, the spatially and temporally continuous sampling, and the very fine vertical resolution enable us to decipher various intrusion cases that can affect differently the biogeochemical responses. The vertical temperature profiles near the strait show thin intermittent layers (occupying a density space of approximately 0.2 σ); the temperature difference between layers is ~0.5 °C (Fig. 7a, see the first "+" symbol along the floats' trajectory in Fig. 1 for the position of this profile). Shortly after the first intrusion was recorded by the float WMO-7900592 (see Fig. 2), the vertical oxygen profile revealed a drop to almost zero at σ ~16.1 and a number of oxygen intrusions down to σ ~17.8. The individual temperature and oxygen profiles were not fully correlated, and the temperature intrusions reached slightly deeper because the propagation of oxygen signals depends not only

on its transport and diffusion, but also on consumption. The basic findings here are that (1) the $b_{bp}(532)$ maximum was "fixed" close to the onset of suboxic zone, which is identified by the deepest oxygen intrusion, and (2) intrusive

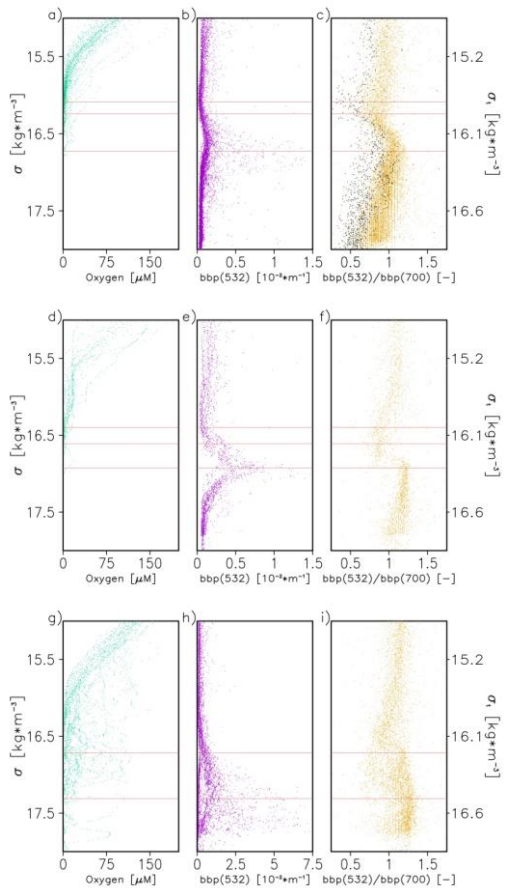

Figure 6. Scatter plots of the oxygen (a, d, g), b_{bp} *(532)* (b, e, h) and S-index (c, f, i). (a, b, c) is for the float WMO-7900591; (d, e, f) is for the float WMO-7900592 downstream of the second diamond (red) along its trajectory in Fig. 1 (after 23-Mar-2014); (g, h, i) is for the remaining records from the float WMO-7900592 (when operating in the area of the Bosporus Straits). The black symbols in (c) are records between 16-May-2015 and 24-Jul-2015).

layers occupy a very broad density interval. These cases are typical for intrusions from the strait.

The correlation between the temperature and oxygen can also be very clearly seen at larger distances from the strait. The profiles in Fig. 7b were recorded two weeks after those in Fig. 7a (see the second "+" symbol along

the floats' trajectory). Remarkably, the distance (in density coordinates) between the $b_{bp}(532)$ maxima is almost the same as that between the temperature and oxygen maxima. However, pronounced $b_{bp}(532)$ maxima are only observed in the anoxic layer, which is below the depth of the deepest oxygen intrusion.

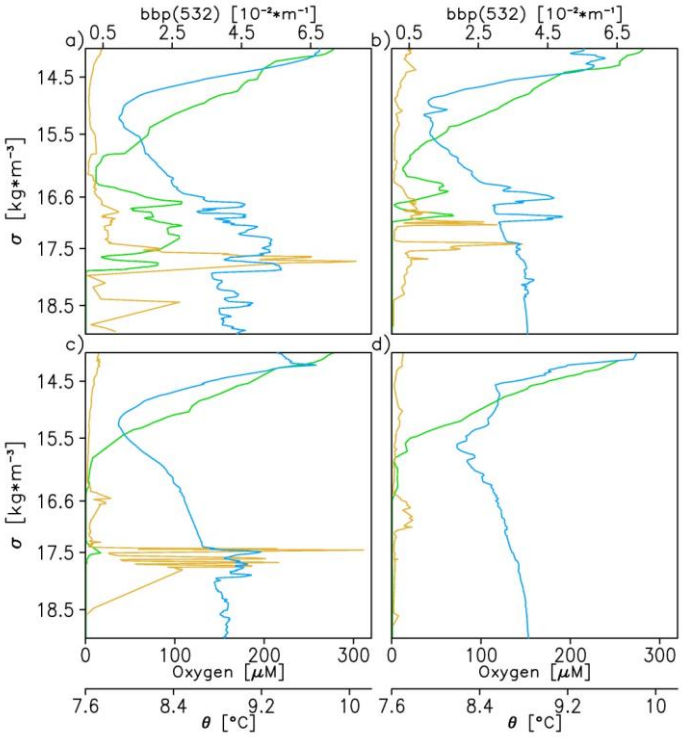

Figure 7. Four cases that illustrate the appearance of temperature intrusions (blue) and the responses of the oxygen (green) and b_{bp}(532) (orange) as observed by the float WMO-7900592: (a)-30-Dec-2013, (b)-13-Jan-2014, (c)-20-Jan-2014, and (d)-05-Sep-2014. See the "+" symbols on the floats' trajectory in Fig. 1 for the positions of these profiles.

A second specific case is demonstrated by the extremely strong interleaving that is observed on 20-Jan-2014 and in some other profiles (not shown here). Multiple temperature intrusions fill the density space between 17.4 and 17.9 σ, which is between 200 m and 300 m (Fig. 7c). Traces of oxygenated water are found at approximately σ=17.5, which corresponds to approximately 240 m, much deeper than the upper boundary of the suboxic zone. However, the $b_{bp}(532)$ peaks more than five times within a density interval of only 0.2 σ, which corresponds to a layer thickness of approximately 15-20 m.

The third typical case considered here is represented in Fig. 7d by the profile that was recorded on 5-Sep-2014. In this case, the temperature intrusions are seen around the core of the CIL; small but measurable oxygen concentrations extend vertically from σ =15.75 to σ =16.5, below the level where the oxygen first reaches zero. Below σ=16.5, $b_{bp}(532)$ increases, but this positive $b_{bp}(532)$ anomaly does not have a counterpart in the temperature distribution. The missing correlation between the temperature and $b_{bp}(532)$ in many other similar profiles (not shown here) indicates that the backscatter maximum is not obligatory caused by thermohaline intrusions. One candidate to explain this feature is the lateral transport in a relatively homogeneous (with respect to temperature and salinity) water mass, where the biogeochemical properties show large contrasts. This possibility is seen by a comparison between the temporal (and spatial) gradients in Fig. 5 at the depth of the suboxic zone and the upper portion of the anoxic zone. We can observe almost uniform temperature and salinity and, at the same time, pronounced $b_{bp}(532)$ gradients. Thus, the advection and available gradients of the biogeochemical properties at this location could induce intense chemoautotrophic activity.

In conclusion, the large variety of intrusions (not only intrusions that are directly linked to the Bosporus inflow) can affect differently the chemoautotrophic activity depending on the type of intrusion. Further research is needed to evaluate the possible clustering of different intrusions to several dominant regimes and understand the role of dynamics of multiple intrusive layers for the biological production in the Black Sea.

4 Conclusions

We studied intrusions from the Bosporus Straits and the open ocean to examine the possible interplay between physical and biogeochemical fields in the Black Sea. Our analysis focused on the characterization and further understanding of the temporal and spatial evolution of the backscattering coefficient and its spectral dependency.

Previous studies used a very limited amount of data, but these chemical and biological data enabled us to quantify important properties and production rates. The use of oxygen optodes, chlorophyll fluorometers, and backscattering sensors in this study is novel because these devices provide a useful proxy for the suspended particle content and a proxy for the size distribution alongside very fine profiling with a resolution of ~1 m and multiple parameters. However, the backscatter sensors did not allow us to fully quantify the biological and chemical characteristics. Therefore, we largely referred to previous studies to reveal the similarities between the data that were analyzed here and previous absolute estimates. The BGC-Argo float data supported these earlier findings and provided our first assessment of the biogeochemistry over large areas of the Black Sea over almost three years of continuous observations. This comparative analysis of large data sets (BGC-Argo) and local chemical/biological observations demonstrated a first step to describe the temporal-spatial dynamics of the Black Sea's biogeochemical system.

Our observations showed that a drastic change in both the thermal and $b_{bp}(532)$ states appeared in the area north and east of the Bosporus Straits. These intrusions created a warm intermediate layer, which was known from the study by Murray et al. [1991], and increased the backscattering coefficient in the pycnocline down to the

ultimate depth of penetration of the Bosporus inflow, which was deeper than 700 m (see Fig. 2; another example of penetration deeper than 700 m is provided in Murray et al. [1991]). These massive intrusions were accompanied by an increase in the thickness of the zone with a high level of backscattering (see the right side of Fig. 4c). This suggests high bacterial abundances with higher intensity near the coast because of more vigorous redox cycling. Most of the $b_{bp}(532)$ maxima were only observed in the anoxic layers, which were below the depth of the deepest oxygen intrusion.

The $b_{bp}(532)$ maximum shoaled rapidly further eastward, approximately along the continental slope, which suggests that the direct effects of sinking in the inflow area did not propagate far from the strait. This conclusion was also supported by the temperature. However, $b_{bp}(532)$ showed very different propagation pathways downstream. While the origin of the temperature and $b_{bp}(532)$ maxima was the same in the Bosporus inflow area, their further evolution was controlled by different processes. In contrast to the temperature, the core of the $b_{bp}(532)$ maximum became shallower with increasing distance from the inflow area.

The BGC-Argo observations clearly demonstrated that the abundance of particles in the deep layers increased dramatically as the oxygen tended towards zero, that is, the $b_{bp}(532)$ maximum was "fixed" close to the onset of the suboxic zone. The $b_{bp}(532)$ values were approximately five times larger in the inflow area than elsewhere, which supports the limited number of observations from Konovalov et al. [2003], who claimed that the maximum concentration of particulate manganese was three to six times higher in the southwestern area of this sea than in the northern and central areas.

The dominance of smaller particles in the suboxic zone became well pronounced; the S-index reached a maximum approximately where the particles' concentration was the highest. A slow increase in the relative amount of larger particles was observed in the upper portion of the anoxic zone. The particle-size distribution shifted in the σ_t interval from 15.8-16.1 (in the open ocean) to 16.0-16.2 along the southern coast (see Fig. 6), which indicated a shift in the position of the suboxic zone with distance from the coast. This temporal-spatial variability illustrated the dynamics of particulate matter, which were interpreted as associated with physical processes, the manganese transformation cycle and bacterial activity. The different vertical variability of the particle concentration and the size distributions in different locations could be considered an illustration of complex biogeochemical processes. Thus, our analysis of the S-index and $b_{bp}(532)$ was a useful tool to identify spatial and temporal sorting from physical and biogeochemical processes.

One novel aspect of this study was its focus on different types of intrusions, which were sampled with a very high vertical resolution. The first type of intrusion, which was associated with the Bosporus inflow, has been addressed in many previous studies. This intrusion was identified by the deepest oxygen intrusion within a very broad density interval (Fig. 2 and Fig. 7a). The interleaving became the dominant process of the propagation of the temperature signal with increasing distance from the straits. $b_{bp}(532)$ almost "matched" the temperature (and oxygen) signal, but its profile was "shifted" in the vertical with respect to the temperature signal, such that pronounced $b_{bp}(532)$ maxima were only observed in the anoxic layers, below the depth of the deepest oxygen intrusion. One of the most interesting intrusions (Fig. 7c) traced oxygenated water deeper than the upper boundary of the suboxic zone. Another remarkable characteristic of these intrusions shown in Fig. 7c revealed multiple

694 $b_{bp}(532)$ maxima with thicknesses of only 15-20 m. In some profiles, the $b_{bp}(532)$ anomalies did not have a
695 counterpart in the temperature distribution; this usually occurred far from the strait and were relatively homogeneous
696 with respect to the temperature and salinity water mass. Advection and large contrasts in the biogeochemical
697 properties at this location could induce intense chemoautotrophic activity. These different types of intrusions (not
698 only those that were directly linked to the Bosporus inflow), individually and in combination, are expected to
699 represent a key process that supports the dynamics of multiple layers of biological production in the Black Sea.
700 Although the focus of this study was on the oxycline, suboxic zone and upper portion of the anoxic zone,
701 some valuable results concerning the upper mixed layer and the CIL should be summarized. The *Chla* and $b_{bp}(532)$
702 values did not follow the patterns that were known from the open ocean, where both fields generally co-vary within
703 the first order [Loisel et al., 1998; Huot et al., 2008]. This observation clearly supports that the $b_{bp}(532)$ in the Black
704 Sea was not solely driven by biogenic (phytoplankton) particles but also by lithogenic particles, or that a
705 phytoplankton species succession, e.g., diatoms *vs.* coccolithophorids [e.g., Mikaelyan et al., 2015], was responsible
706 for these specific features. However, the low concentration of particles and lower [Chla] during the extremely warm
707 2016 indicated an overall positive correlation between the two properties. This change in the biogeochemical
708 properties was likely a response to temperature changes, which should motivate a deeper analysis of the observed
709 warming of 1°C in the CIL over the past 3-4 decades and the resulting biogeochemical response.
710 Following earlier analyses (e.g., Oguz et al., 2006), which primarily focused on the upper ocean's
711 biogeochemical responses, we should address the evolution at the depth of the suboxic and anoxic zones. The
712 continuously recorded changes during the last three years (Figs. 4d, 5d) provide strong motivation to differentiate
713 among temporal or spatial changes that are associated with the displacement of the float, local changes, and the
714 possible drift of the instrumentation. This future development could bridge BGC-Argo observations (providing a
715 large amount of b_{bp} data but only indirectly describing the biogeochemical properties) and precise (but limited)
716 biogeochemical ship observations. This approach could facilitate using BGC-Argo floats to map the temporal and
717 spatial variability of heterotrophic bacteria.
718

719

720 **Acknowledgments and Data**

721 We are grateful to V. Slabakova for the work that was performed during the deployment of the floats and to P.M.
722 Poulain for coordinating the Argo activities in the Black Sea. We are grateful to J. Murray for his useful suggestions
723 on improving the paper. EVS acknowledges support from the EC grant 312642 and Hervé Claustre from the
724 European Research Council for the Remotely Sensed Biogeochemical Cycles in the Ocean (remOcean) project
725 (grant agreement 246777). Data that support the analysis and conclusions can be found at
726 http://www.ifremer.fr/co-argoFloats/float?detail=false&ocean=A&lang=en&techChart=false&ptfCode=7900591
727 and
728 http://www.ifremer.fr/co-argoFloats/float?detail=false&ocean=A&lang=en&techChart=false&ptfCode=7900592

The data that support the findings of this study are available from ftp://ftp.ifremer.fr/ifremer/argo/dac/coriolis/6901866/ .

??????????????

References

Anderson, G.C., 1969. Subsurface chlorophyll maximum in the Northeast Pacific Ocean.Limnology and Oceanography. 14 (3), 386–391.

Balch, W.M., Drapeau, D., Fritz, J., Bowler, B. and Nolan, J., 2001. Optical backscattering in the Arabian Sea- continuous underway measurements of particulate inorganic and organic carbon. Deep Sea Research I, 48: 2423-2452.

Blatov, A. S., N. P. Bulgakov, V. A. Ivanov, A. N. Kosarev, and V. S. Tujilkin (1984), *Variability of Hydrophysical Fields in the Black Sea* [in Russian], 240 pp., Gidrometeoizdat, Leningrad.

Boss, E., and W. S. Pegau (2001), The relationship of light scattering at an angle in the backward direction to the backscattering coefficient, Appl. Opt., 40, 5503–5507.

Boss, E., D. Swift, L. Taylor, P. Brickley, R. Zaneveld, S. Riser, M. J. Perry, and P. G. Strutton (2008), Observations of pigment and particle distributions in the western North Atlantic from an autonomous float and ocean color satellite, Limnol. Oceanogr. Methods, 53, 2112–2122.

Brewer, P.G., and D.W. Spencer (1974). Distribution of some trace elements in Black Sea and their flux between dissolved and particulate phases. In: Degens, E.T., Ross, D.A. (Eds.), The Black Sea - Geology, Chemistry and Biology. Am. Assoc. Pet. Geol. Mem. 20, 137-143.

Claustre, H., et al. (2010), Bio-optical profiling floats as new observational tools for biogeochemical and ecosystem studies, in Proceedings of the "OceanObs'09: Sustained Ocean Observations and Information for Society" Conference, Venice, Italy, 21–25 Sep., vol. 2, edited by J. Hall, D. E. Harrison, and D. Stammer, ESA Publ. WPP-306, doi:105270/OceanObs09.cwp.17.

Cociasu, A., V. Diaconu, L. Popa, I. Nae, L. Buga, L. Dorogan & V. Malciu, 1997. Nutrient stock of the Romanian shelf of the Black Sea in the last three decades. In E. Ozsoy & A. Mikaelyan (eds), Sensitivity to change: Black Sea, Baltic and North Sea. NATO ASI Series, Kluwer Academic Publishers 27: 49–63.

Codispoti, L.A, G.E. Friederich, J.W. Murray, and C.IVL Sakamoto, Chemical variability in the Black Sea: Implications of continuous vertical profiles that pmetrated the oxic/anoxic interface, Deep Sea Res., 38, suppl.,S 691-S710, 1991.

Fuchsman, C.A., Murray, J.W., and Staley, J.T. (2012) Stimulation of autotrophic denitrification by intrusions of the Bosporus Plume into the anoxic Black Sea. Frontiers in Aquatic Microbiology 3: 257.Gregg, M. C., and E. Ozsoy, Mixing on the Black Sea shelf north of the Bosphorus, Geophys. Res. Lett., 26, 1869–1872, 1999

764 Grégoire, M. and Soetaert, K. E. R. (2010), Carbon, nitrogen, oxygen and sulfide budgets in the Black Sea: a
765 biogeochemical model of the whole water column coupling the oxic and anoxic parts, Ecol. Model., 221,
766 2287–2301.

767 Gruber N. (2011), Warming up, turning sour, losing breath: ocean biogeochemistry under global change.
768 Philosophical Transactions of the Royal Society a-Mathematical Physical and Engineering Sciences,
769 369(1943):1980-96.

770 Huot, Y, Morel A, Twardowski MS, Stramski D, Reynolds RA. (2008), Particle optical backscattering along a
771 chlorophyll gradient in the upper layer of the eastern South Pacific Ocean. Biogeosciences. 5:495-507.

772 International Ocean-Color Coordinating Group (IOCCG) (2011), Bio-optical sensors on Argo floats, vol. 11, edited
773 by H. Claustre, Darthmouth, Canada.

774 Jannasch, H.W., Wirsen, C.O., Molyneaux, S. (1991), Chemoautotropic sulfur oxidizing bacteria from the Black
775 Sea. Deep-Sea Research 38 (Suppl. 2), S1105–S1120.

776 Johnson, K.S.**,** W.M. Berelson, E.S. Boss, Z. Chase, H. Claustre, S.R. Emerson, N. Gruber, A. Körtzinger, M.J.
777 Perry, and S.C. Riser (2009), Observing biogeochemical cycles at global scales with profiling floats and
778 gliders: Prospects for global array. *Oceanography,* **22**: 216-225.

779 Jørgensen, B.B., Fossing, H., Wirsen, C.O., Jannasch, H.W. (1991), Sulfide oxidation in the anoxic Black Sea
780 chemocline. Deep-Sea Research 38 (Suppl. 2), S1083–S1103.

781 Karl, D.M., Knauer, G.A (1991), Microbial production and particle flux in the upper 350 m of the Black Sea. Deep-
782 Sea Research 38 (Suppl. 2), S921–S942.

783 Kempe, S., Diercks, A. R., Liebezeit, G., & Prange, A. (1991), Geochemical and structural aspects of the pycnocline
784 in the Black Sea (R/V Knorr 134-8 Leg 1, 1988). In *Black Sea Oceanography* (pp. 89-110). Springer
785 Netherlands.

786 Kolesnikov, A. (1953), Seasonal course of temperature, stability and vertical turbulent heat exchange in the open
787 part of the Black Sea. Tr. Mor. Gudrol. Inst. USSR AS 3, 3 –13 (in Russian).

788 Konovalov, S. K., Luther, III, G. W., Friederich, G. E., Nuzzio, D. B., Tebo, B. M., Murray, J.W., Oguz, T., Glazer,
789 B., Trouwborst, R. E., Clement, B., Murray, K. J., and Romanov, A. S.(2003), Lateral injection of Oxygen
790 with the Bosporus plume fingers of oxidizing potential in the Black Sea, Limnol. Oceanogr., 48, 2369–
791 2376.

792 Konovalov, S.K. and J.W. Murray (2001), Variations in the chemistry of the Black Sea on a time scale of decades
793 (1960-1995). Journal of Marine Systems 31:217-243.

794 Konovalov, S.K., Murray, J.W., Luther III, G.W. (2005), Basic processes of Black Sea biogeochemistry.
795 Oceanography 18, 24–35.

796 Konovalov, S., Murray, J., Luther, G., and Tebo, B. (2006), Processes controlling the redox budget for the
797 oxic/anoxic water column of the Black Sea, Deep-Sea Res. Pt. II, 53, 1817–1841.

798 Korotaev, G., Oguz, T., and Riser, S. (2006), Intermediate and deep currents of the Black Sea obtained from
799 autonomous profiling floats, Deep Sea Res. Pt. II, 53, 1901–1910.

800 Kostadinov, T. S.; Siegel, D. A. & Maritorena, S. (2009), Retrieval of the particle size distribution from satellite
801 ocean color observations, J. Geophys. Res. 114, C09015.

802 Körtzinger, M.J. Perry & S.C. Riser (2009), Observing biogeochemical cycles at global scales with profiling floats
803 and gliders: Prospects for global array. Oceanography, 22, 216-225.

804 Latif, M. A., E. Ozsoy, T. Oguz and U. Unluata (1991), Observations of the Mediterranean inflow into the Black
805 Sea. Deep-Sea Research,Vol. 38, Suppl 2. pp. 5711-5723, 1991.

806 Lewis, B.L., Landing, W.M., 1991. The biogeochemistry of manganese and iron in the Black Sea. Deep-Sea
807 Research 38 (Suppl. 2A), S773–S804.

808 Loisel, H., and A. Morel (1998), Light scattering and chlorophyll concentration in case 1 waters: A reexamination,
809 Limnol. Oceanogr., 43, 847–858.

810 Loisel H, Nicolas JM, Sciandra A, Stramski D, Poteau A. (2006), Spectral dependency of optical backscattering by
811 marine particles from satellite remote sensing of the global ocean. Journal of Geophysical Research-
812 Oceans. C09024, doi:10.1029/2005JC003367

813 Loisel, H., et al. (2011), Characterization of the bio-optical anomaly and diurnal variability of particulate matter, as
814 seen from scattering and backscattering coefficients, in ultra-oligotrophic eddies of the Mediterranean Sea,
815 Biogeosciences, 8, 3295–3317.

816 Lorthiois T, Doxaran D, Chami M (2012), Daily and seasonal dynamics of suspended particles in the Rhône River
817 plume based on remote sensing and field optical measurements. Geo-Mar Lett 32(2):89–102.

818 Mignot, A., H. Claustre, J. Uitz, A. Poteau, F. D'Ortenzio, and X. Xing (2014), Understanding the seasonal
819 dynamics of phytoplankton biomass and the deep chlorophyll maximum in oligotrophic environments: A
820 Bio-Argo float investigation, Global Biogeochem. Cycles, 28, 856– 876, doi:10.1002/2013GB004781.

821 Mikaelyan, A.S., Pautova, L.A., Chasovnikov, V.K., Mosharov, S.A. & V.A. Silkin (2015), Alternation of diatoms
822 and coccolithophores in the north-eastern Black Sea: a response to nutrient changes, Hydrobiologia, 755(1),
823 89-105

824 Morel, A., and Y. H. Ahn (1991), Optics of heterotrophic nanoflagellates and ciliates: A tentative assessment of
825 their scattering role in oceanic waters compared to those of bacterial and algal cells, J. Mar. Res., 49, 177–
826 202.

827 Morel, A., and S. Maritorena (2001), Bio-optical properties of oceanic waters: A reappraisal, J. Geophys. Res., 106,
828 7163–7180.

Morgan, J.A., Quinby, H.L., Ducklow, H.W. (2006), Bacterial abundance and production in the western Black Sea. Deep-Sea Res. II, 53, 1945–1960.

Murray, J. W., L. A. Codispoti, and G. E. Friederich (1995), Oxidationreduction environments: The suboxic zone in the Black Sea, in *Aquatic Chemistry: Interfacial and Interspecies Processes,* Adv. Chem. Ser., vol. 224, edited by C. P. Huang, C. R. OMelia, and J. J. Morgan, pp. 157–176, American Chemical Society, Washington, D.C.

Murray, J.W., Jannasch, H.W., Honjo, S., Anderson, R.F., Reeburgh, W.S., Top, Z., Friederich, GE., Codispoti, L.A., Izdar, E. (1989), Unexpected changes in the oxic/anoxic interface in the Black Sea. Nature 338, 411-413.

Murray, J.W., Top, Z. and Ozsoy, E., (1991), Hydrographic properties and ventilation of the Black Sea. Deep-Sea Res., 38: S663-S689.

Oguz, T., J. W. Dippner, Z. Kaymaz (2006), Climatic Regulation of the Black Sea hydro-meteorological and ecological properties at interannual-to-decadal time scales. J. Marine Systems, 60,235-254.

Organelli, E., and Coauthors, 2016:Anovel near-real-time qualitycontrol procedure for radiometric profiles measured by Bio-Argo floats: Protocols and performances. J. Atmos. Oceanic Technol., 33, 937–951, doi:10.1175/JTECH-D-15-0193.1.

Ozsoy, E., Iorio, D. D., Gregg, M., Backhaus, J., 2001. Mixing in the Bosphorus Strait and the Black Sea Continental Shelf: Observations and a Model of the Dense Water Outow. J. Mar. Sys. 31, 99-135.

Özsoy, E., Unluata, U., Top, Z. (1993), The evolution of Mediterranean water in the Black Sea: interior mixing and material transport by double diffusive intrusions**.** *Progress in Oceanography, 31, 3, 275-320.*

Ovchinnikov, I.M., Popov, Y.I. (1987), Evolution of the cold intermediate layer in the Black Sea. Oceanology 27,555–560.

Röttgers, R. and B. P. Koch (2012), Spectroscopic detection of a ubiquitous dissolved pigment degradation product in subsurface waters of the global ocean, Biogeosciences, 9, 2585–2596.

Rozanov, A.G., Neretin, L.N., Volkov, I.I. (1998), Redox nepheloid layer (RNL) of the Black Sea: its location, composition and origin. In: Ivanov, L.I., Oguz, T. (Eds.), Ecosystem Modeling as a Management Tool for the Black Sea, Vol. 1. Kluwer Academic Publishers, Amsterdam, pp. 77–91.

Schmechtig, C., Poteau, A., Claustre, H., D'Ortenzio, F., Dall'Olmo, G., Boss, E. (2015), Processing Bio-Argo particle backscattering at the DAC level. http://dx.doi.org/10.13155/39459

Schmechtig, C., Poteau, A., Claustre, H., D'Ortenzio, F., Boss, E. (2015), Processing Bio-Argo chlorophyll-a concentration at the DAC level. http://dx.doi.org/10.13155/39468

Schmechtig, C., Claustre, H., Poteau, A., D'Ortenzio, F. (2014), Bio-Argo quality control manual for the Chlorophyll-A concentration. http://dx.doi.org/10.13155/35385

Sullivan , J. M., & M. S. Twardowski (2009), Angular shape of the volume scattering function in the backwards direction. Applied Optics, 48(35):6811–6819.

Spencer D.W. and Brewer P.G. (1971), Vertical advection diffusion and redox potentials as controls on the distribution of manganese and other trace metals dissolved in waters of the Black Sea. Journal of Geophysical Research, 76, 5877-5892.

Stanev, E. V. (2005), Understanding Black Sea dynamics: overview of recent numerical modelling, Oceanography, 18, 56–75.

Stanev, E. V., He, Y., Grayek, S., and Boetius, A. (2013), Oxygen dynamics in the Black Sea as seen by Argo profiling floats, Geophys. Res. Lett., 40, 3085–3090, doi:10.1002/grl.50606, 2013.

Stanev, E.V., J.A Simeonov, and E.L. Peneva. 2001. Ventilation of Black Sea pycnocline by the Mediterranean plume. Journal of Marine Systems, 31:77-97.

Stanev, E. V., He, Y., Staneva, J., and Yakushev, E. (2014), Mixing in the Black Sea detected from the temporal and spatial variability of oxygen and sulfide – Argo float observations and numerical modelling, Biogeosciences, 11, 5707-5732, doi:10.5194/bg-11-5707-2014, 2014.

Stanev, E. V., Staneva, J., Bullister, J. L., and Murray, J. W. (2004), Ventilation of the Black Sea pycnocline. parameterization of convection, numerical simulations and validations against observed chlorofluorocarbon data, Deep-Sea Res., 51, 2137–2169.

Stramski, D., and D. A. Kiefer (1991), Light scattering by microorganisms in the open ocean, Prog. Oceanogr., 28, 343–383.

Tolmazin, D. (1985), Changing coastal oceanography of the Black Sea. I: northwest shelf. Prog. Oceanogr., 15, 217-276.

Twardowski, M. S., E. Boss, J. B. Macdonald, W. S. Pegau, A. H. Barnard, and J. R. V. Zaneveld (2001), A model for estimating bulk refractive index from the optical backscattering ratio and the implications for understanding particle composition in case I and case II waters, J.Geophys. Res., 106, 14,129–14,142.

Ulloa, O., S. Sathyendranath, and T. Platt (1994), Effect of the particle-size distribution on the backscattering ratio in seawater, Appl. Opt., 30, 7070–7077.

DeVries, T., Liang, J.-H., and Deutsch, C.: A mechanistic particle flux model applied to the oceanic phosphorus cycle, Biogeosciences, 11, 5381-5398, doi:10.5194/bg-11-5381-2014, 2014.

Wakeham, S.G.; Amann, R.; Freeman, K.H.; Hopmans, E.C.; Jørgensen, B.B.; Putnam, I.F.; Schouten, S.; Sinninghe Damsté, J.S.; Talbot, H.M. & Woebken, D. (2007). Microbial Ecology of the Stratified Water Column of the Black Sea as Revealed by a Comprehensive Biomarker Study. *Organic Geochemistry*, Vol. 38, No. 12, 2070–2097.

White G., M. Relander, J. Postal and J. W. Murray (1989), *Hydrographic data from the* 1988 *Black Sea Oceanographic Expedition,* Special report *(*School of Oceanography, College of Ocean and Fishery Sciences, University of Washington), no 109, 34pp.

Xing, X., H. Claustre, J. Uitz, A. Mignot, A. Poteau, and H. Wang (2014), Seasonal variations of bio-optical properties and their interrelationships observed by Bio-Argo floats in the subpolar North Atlantic, J. Geophys. Res. Oceans, 119, doi:10.1002/ 2014JC010189.

Xing, X., Morel, A., Claustre, H., D'Ortenzio, F., and A. Poteau (2012), Combined processing and mutual interpretation of radiometry and fluorometry from autonomous profiling Bio-Argo floats: 2. Colored dissolved organic matter absorption retrieval. *Journal of Geophysical Research*, Vol. 117, No. C4, C04022, http://dx.doi.org/10.1029/2011JC007632.

Yakushev, E. V., Pollehne, F., Jost, G., Kuznetsov, I., Schneider, B., and Umlauf, L. (2007), Analysis of the water column oxic/anoxic interface in the Black and Baltic seas with a numerical model, Mar. Chem., 107, 388–410.

Yilmaz, A., Tuğrul, S., Polat, C., Ediger, D., Çoban, Y., and E. Morkoç (1998), On the production, elemental composition (C, N, P) and distribution of photosynthetic organic matter in the Southern Black Sea. Hydrobiologia. 363(1):141–155.

Yilmaz, A., Coban-Yildiz, Y., Telli-Karakoc, F., Bologa, A., (2006), Surface and mid-water sources of organic carbon by photoautotrophic and chemoautotrophic production in the Black Sea. Deep Sea Research II 53, 1988-2004.

Figure 1. Trajectories (black lines) of the floats WMO-7900591 (1 in the figure) and WMO-7900592 (2 in the figure). The dots identify the surfacing position, and their colors are specified to approximately represent seasonal changes in the SST, which can be easily translated into time (color bar). This coarse presentation of the "timing" is used to avoid numbering all the surface positions and to display the chronology of the observations. The launching positions and times are also provided. The small white dots on the surface positions of WMO-7900592 (white dots with blue outlines) identify portions of the trajectory for which more detailed analysis is provided in the text. The diamond symbols identify the positions, time (in addition to the day after 1-Jan-2014) and profile number on the trajectories, which are mentioned in the text. WMO-7900591: diamond (blue), 16-Mar-2015; diamond (green), 15-May-2015; WMO-7900592: diamond (black), 22-Dec-2013; diamond (red), 23-Mar-2014. Four coordinates along the trajectory of float WMO-7900592 have been marked by "+" to identify its positions on 30-Dec-2013, 13-Jan-2014, 20-Jan-2014, and 05-Sep-2014 where data are discussed further in the text.

Figure 2. Depth versus time profiles of the temperature (a) and $b_{bp}(532)$ (b) that were measured by WMO-7900592. The diagram shows data for only one portion of the trajectory (Fig. 1), with the small dots in the middle of the larger dots (in color) showing the surface positions. The black diamond along the trajectory is for 26-Dec- and identifies an outbreak of particle concentrations and positive temperature anomalies. The time of this outbreak is identified in the figures by the time of first appearance of higher temperature over depth interval of more than 300 m.

Figure 3. Time versus depth diagrams of the temperature (a), salinity (b) and density (c). The longer-time diagram (left) is from WMO-7900591, and the shorter diagram (right) is from WMO-7900592; the latter terminated earlier its operation. Additional isolines were plotted to more clearly present the temporal evolution in zones where the color resolution is insufficient: 8.25, 8.5, and 8.75 °C for the temperature; 19.9 for the salinity, which is approximately the bottom of the CIL; and 1015.5 kg/m^3 for the density, which is also approximately the bottom of the CIL. The outcropping isolines that are plotted with red (8.25°C) approximately illustrate the location and timing of cold water formation.

Figure 4. Time versus depth diagrams of oxygen (a), [Chla] (b), $b_{bp}(532)$ (c) and the ratio of $b_{bp}(532)$ versus $b_{bp}(700)$ (d). The vertical white strips identify times when the data quality was poor. Additional isolines were plotted for the oxygen to more clearly present the temporal evolution in zones where the color resolution is insufficient: 5 µM (red) and 50 µM (white). These isolines are repeated in some other plots to facilitate the identification of similarities and differences in the temporal evolution of different variables in the areas around the suboxic zone. The Chla diagrams are plotted down to the upper boundary of the suboxic zone (see the explanation in section 2).

Figure 5. Same as in Fig. 4, but plotted against density.

Figure 6. Scatter plots of the oxygen (a, d, g), b_{bp} *(532)* (b, e, h) and S-index (c, f, i). (a, b, c) is for the float WMO-7900591; (d, e, f) is for the float WMO-7900592 downstream of the second diamond (red) along its trajectory in Fig.

1 (after 23-Mar-2014); (g, h, i) is for the remaining records from the float WMO-7900592 (when operating in the area of the Bosporus Straits). The black symbols in (c) are records between 16-May-2015 and 24-Jul-2015).

Figure 7. Four cases that illustrate the appearance of temperature intrusions (blue) and the responses of the oxygen (green) and $b_{bp}(532)$ (orange) as observed by the float WMO-7900592: (a)-30-Dec-2013, (b)-13-Jan-2014, (c)-20-Jan-2014, and (d)-05-Sep-2014. See the "+" symbols on the floats' trajectory in Fig. 1 for the positions of these profiles.